



Self-gated MRI motion modeling for respiratory motion compensation in integrated PET/MRI



Robert Grimm^{a,b,*}, Sebastian Fürst^c, Michael Souvatzoglou^c, Christoph Forman^{a,b}, Jana Hutter^a, Isabel Dregely^c, Sibylle I. Ziegler^c, Berthold Kiefer^b, Joachim Hornegger^a, Kai Tobias Block^d, Stephan G. Nekolla^c

^a Pattern Recognition Lab, FAU Erlangen-Nürnberg, Erlangen, Germany

^b Siemens AG Healthcare MR, Erlangen, Germany

^c Department of Nuclear Medicine, Klinikum Rechts der Isar, Technische Universität München, Munich, Germany

^d Department of Radiology, NYU Langone Medical Center, New York, NY, USA

ARTICLE INFO

Article history:

Received 31 May 2014

Received in revised form 27 August 2014

Accepted 30 August 2014

Available online 30 September 2014

Keywords:

Respiratory motion
Motion compensation
PET/MRI
MRI
Respiratory gating

ABSTRACT

Accurate localization and uptake quantification of lesions in the chest and abdomen using PET imaging is challenged by respiratory motion occurring during the exam. This work describes how a stack-of-stars MRI acquisition on integrated PET/MRI systems can be used to derive a high-resolution motion model, how many respiratory phases need to be differentiated, how much MRI scan time is required, and how the model is employed for motion-corrected PET reconstruction. MRI self-gating is applied to perform respiratory gating of the MRI data and simultaneously acquired PET raw data. After gated PET reconstruction, the MRI motion model is used to fuse the individual gates into a single, motion-compensated volume with high signal-to-noise ratio (SNR). The proposed method is evaluated in vivo for 15 clinical patients. The gating requires 5–7 bins to capture the motion to an average accuracy of 2 mm. With 5 bins, the motion-modeling scan can be shortened to 3–4 min. The motion-compensated reconstructions show significantly higher accuracy in lesion quantification in terms of standardized uptake value (SUV) and different measures of lesion contrast compared to ungated PET reconstruction. Furthermore, unlike gated reconstructions, the motion-compensated reconstruction does not lead to SNR loss.

© 2014 Elsevier B.V. All rights reserved.

1. Introduction and purpose

Typical scan durations for positron emission tomography (PET) imaging of the lung and abdomen vary between two and ten minutes per bed position. Due to the long acquisition time, breath-hold techniques cannot be applied to manage respiratory motion. Respiratory-gating approaches have the drawback of discarding data, resulting in reduced signal-to-noise ratio (SNR) or prolonged scan time. Further, the implementation of respiratory gating is challenging, e.g., in cardiac imaging, where the scan efficiency is already reduced by ECG gating. Therefore, artifacts due to respiratory motion are frequently seen in clinical PET/MRI protocols. These artifacts can be categorized into two groups: Firstly, there is a mismatch between the MR-based attenuation correction map (μ -map) and the PET image. The former is typically acquired in an end-expiratory breath-hold, while the latter is acquired during free breathing. The

anatomical mismatch causes regionally varying under- or overestimation of tracer activity, especially in the vicinity of the diaphragm (Keller et al., 2013; Buerger et al., 2012b), resulting in inaccurate uptake quantification. Secondly, respiration leads to local image blurring (smearing) along the direction of motion, i.e., primarily in the cranio-caudal direction. This can result in an incorrectly estimated volume, shape, and apparent tracer uptake of lesions (Liu et al., 2009; Geramifar et al., 2013; Nehmeh et al., 2002; Bundschuh et al., 2008; Würslin et al., 2013) as well as in reduced conspicuity of small lesions.

Respiration is a predominantly periodic type of motion that can be compensated for if a model of the motion is available. Typically, this model is manifested as displacement vector fields describing the nonrigid deformation that maps voxels between different respiratory states. A comprehensive review of respiratory motion models has recently been published by McClelland et al. (2013).

On integrated PET/MRI scanners that recently became available (Delso et al., 2011), PET motion compensation can be achieved using MR data. Respiratory motion models are formed either by

* Corresponding author at: Siemens AG Healthcare MR, Erlangen, Germany.
E-mail address: robertgrimm@siemens.com (R. Grimm).

fast MRI sequences (Buerger et al., 2012b; Dikaïos et al., 2012; King et al., 2012) or by retrospective gating and averaging over multiple respiratory cycles (Würslin et al., 2013; Buerger et al., 2012a; Ouyang et al., 2013; Huang et al., 2013). While the use of fast imaging techniques allows to capture complete volumes within 0.4–0.7 s, spatial resolution and SNR are compromised. Gated reconstructions, on the other hand, usually provide better image quality but are unable to reflect inter-cycle variations in the respiration pattern.

In both cases, the MRI scan can be conducted (1) with only short acquisition time or (2) throughout the whole PET acquisition. Approach (1) relies on a physiological surrogate signal (e.g., a respiratory bellows) that must be available for the entire PET scan and has to be mapped reliably to the respiratory gates of the MRI acquisition. While this method cannot account for a later drift in respiratory amplitude, approach (2) prohibits the acquisition of other diagnostic MRI images in parallel to the PET scan.

Retrospectively gated MRI motion models can further be subdivided into three categories according to the acquisition method: Displacement fields can be measured (a) directly using tagged MRI (Ouyang et al., 2013; Guérin et al., 2011; Chun et al., 2012), or the volume can be sampled using (b) a 2D multi-slice technique (Würslin et al., 2013; Dikaïos et al., 2012; Dutta et al., 2013) or (c) using a 3D acquisition (Dikaïos et al., 2012; Buerger et al., 2012a; Grimm et al., 2013b). The displacements are estimated with the help of deformable image registration methods.

The correspondence between the motion model and the patient motion is established through a physiological signal surrogate. Often, 1D navigator echoes (Würslin et al., 2013; Ouyang et al., 2013; Dutta et al., 2013) are interleaved with the image acquisition. If the imaging sequence itself generates a physiological signal, the term self-gating is used (Buerger et al., 2012b; Grimm et al., 2013b). Other options include an external sensor that is attached to the patient, such as respiratory bellows or belts (Chun et al., 2012), and 2D or 3D navigator acquisitions (King et al., 2012).

The MRI-derived motion model can be applied to the PET data in different ways to compensate for motion. Two important groups of algorithms for non-rigid motion correction are commonly distinguished in the literature (Rahmim et al., 2013; Dikaïos et al., 2012; Ouyang et al., 2013; Lamare et al., 2007; Polycarpou et al., 2012):

1. *Motion-compensated image reconstruction (MCIR)*: The motion field is incorporated directly into the PET reconstruction process, e.g., by adapting the system matrix (Ouyang et al., 2013; Chun et al., 2012).
2. *Post-reconstruction registration (PRR)*: Each PET gate is first reconstructed using conventional algorithms, then warped to a reference respiratory phase, and finally averaged (Buerger et al., 2012b; Würslin et al., 2013).

Theoretical examinations promise more accurate quantification and improved SNR for MCIR (Lamare et al., 2007; Polycarpou et al., 2012; Dikaïos and Fryer, 2011; Chun and Fessler, 2013; Tsoumpas et al., 2013), but it is generally assumed that PRR provides similar results (Rahmim et al., 2013; Polycarpou et al., 2012) as long as the individual gates contain a comparable and sufficiently high number of counts. The computational complexity of PRR is significantly lower than that of MCIR, and it allows to use clinically established reconstruction algorithms.

According to these characteristic features, the approach for respiratory motion compensation on integrated PET/MRI scanners proposed in this work is classified as follows. It utilizes a radial stack-of-stars 3D MRI pulse sequence. The motion model is acquired during the entire PET acquisition, thereby assuring high spatial fidelity while being able to adapt to changes in the respiratory

pattern. The MRI sequence allows for retrospective self-gating, i.e. a respiratory signal is derived without the need for additional MRI navigator echoes or sensors attached to the patient. The MRI motion model is utilized for motion-corrected PET image reconstruction according to the PRR scheme.

In this work, an extensive evaluation of the self-gated MRI motion model and its utilization in PET image reconstruction is presented. We examine the minimal number of respiratory phases to be differentiated in the MRI motion model, which was chosen between 4 and 8 bins in related work. Moreover, we analyze the required MRI scan time for motion modeling. The efficacy and robustness are validated in a detailed quantitative evaluation, based on a population of 15 patients, which is considerably larger than in previous and related work. Table 1 compares the key features of the present technique against current literature. A proof of concept of our proposed method in three patients was published previously (Grimm et al., 2013b).

2. Materials and methods

Our proposed approach is based on the following workflow for an integrated whole-body PET/MRI scanner. An overview of the individual steps is provided in Fig. 1, and a detailed discussion follows in the subsections.

The μ -maps are acquired with a conventional breath-hold 3D Dixon spoiled GRE scan. Then, the self-gating MRI sequence for motion modeling and the PET list-mode acquisition are carried out simultaneously during free breathing. In this study, a scan duration of 10 min was used.

2.1. Self-gated radial MRI

The respiratory motion model is generated with a prototype implementation of a T1-weighted radial stack-of-stars spoiled 3D gradient-echo sequence with fat suppression (StarVIBE) (Chandarana et al., 2011). It samples k -space in sagittal slab orientation to capture the dominant motion in the readout plane. Slice encoding is performed in a Cartesian manner, as illustrated in Fig. 2. All N_z slice encoding steps are performed for a given radial angle before moving to the next angle. An increment of 111.25° is used for subsequently acquired radial angles. This angle is the golden ratio over 180° (Winkelmann et al., 2007) and distributes the sampling incoherently but approximately uniformly over the readout plane, facilitating retrospectively gated reconstruction (Buerger et al., 2012a; Lin et al., 2008).

The stack-of-stars k -space trajectory allows to derive a self-gating signal (SGS) from the k -space center $k_x = k_y = k_z = 0$ (Lin et al., 2008; Paul et al., 2014). The k -space center is crossed by every readout in the central k -space partition ($k_z = 0$). The mean value of the central three k -space samples in such a readout is taken to compute one sample of the SGS. Thus, with the interleaved slice encoding along k_z , one SGS sample is generated every $N_z \cdot \text{TR}$, where TR is the MRI repetition time and N_z the number of slices. For typical scan protocols, the sampling rate is in the order of 5–10 Hz. The SGS can be determined for all utilized RF receive coils, but not all coil elements reflect the respiratory motion equally well. We use a heuristic method to automatically select a suitable coil element according to a score that favors the signal of a coil element that has a distinct spectral component in the range of expected respiratory frequencies but is not affected by high-frequency variations due to noise or cardiac motion (Grimm et al., 2013a).

To compensate for low-frequency drifts in the signal that can be caused by peristaltic motion and other non-periodic events, a baseline correction is applied by subtracting the signal mean value over

Table 1
Summary of related work on PET/MRI respiratory motion compensation.

Author	Imaging type	MRI sequence	Physiological signal	Compensation method	Evaluation
Dikaios et al. (2012)	Fast/gated MRI	2D/3D	2D navigator/-	PRR/MCIR	Simulations
Ouyang et al. (2013)	Gated MRI	Tagging	1D navigator	MCIR	Phantom, animals
Chun et al. (2012)	Gated MRI	Tagging	Bellows	MCIR	Phantom, animals
Guérin et al. (2011)	Gated MRI	Tagging	Bellows	MCIR	Simulations, phantom
Dutta et al. (2013)	Gated MRI	2D radial	1D navigator	MCIR	1 volunteer
Buerger et al. (2012b)	Fast MRI	3D	1D navigator	PRR	Simulations, phantom
King et al. (2012)	Fast/gated MRI	3D	2D navigator	PRR	Simulations
Tsoumpas et al. (2011)	Fast MRI	3D	1D navigator	PRR/ MCIR	Simulations
Würsli et al. (2013)	Gated MRI	2D	1D navigator	PRR	Phantom, 4 patients
Proposed	Gated MRI	Stack-of-stars	Self-gating	PRR	15 patients

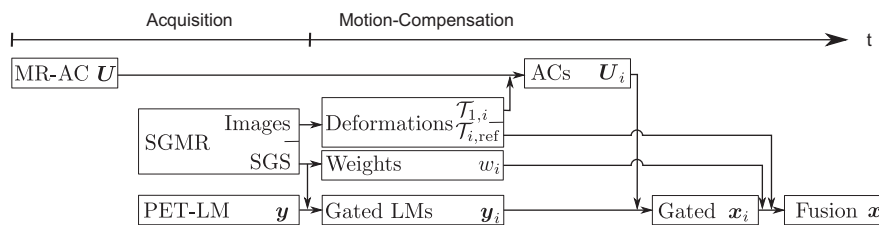


Fig. 1. Overview of the data processing workflow. Firstly, a static MRI attenuation-correction (MR-AC) map \mathbf{U} is acquired in a breath-hold Dixon MRI scan at end-expiration. Afterwards, the self-gating MRI sequence (SGMR) and PET list-mode (PET-LM) acquisition are carried out simultaneously. The SGMR delivers a self-gating signal (SGS) and retrospectively gated image volumes at different respiratory levels (bins). Registration of the phases yields the deformation fields $\mathcal{T}_{1,i}$ and $\mathcal{T}_{i,ref}$ for $i \in \{1, \dots, N_{\text{Bins}}\}$. The SGS is analyzed to compute bin weights w_i . The SGS binning table is also applied to partition the list-mode data \mathbf{y} into gates \mathbf{y}_i . A dynamic MR-AC \mathbf{U}_i is computed from \mathbf{U} and $\mathcal{T}_{1,i}$. Gated PET volumes \mathbf{x}_i are reconstructed from \mathbf{y}_i and \mathbf{U}_i , and fused into a single volume with the help of w_i and $\mathcal{T}_{i,ref}$.

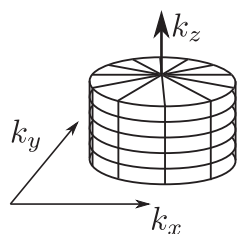


Fig. 2. The stack-of-stars trajectory uses radial sampling for the readout plane $k_x \times k_y$ and Cartesian slice encoding.

a 50 s sliding window. Variable amplitude-based binning (Dawood et al., 2007) is applied to partition the radial readouts into N_{Bins} bins containing equal amounts of data, according to the respective self-gating signal amplitude. This scheme ensures comparable statistics also for the PET list-mode data that are gated in the same manner (see Section 2.3). Since on the utilized PET/MRI system the PET and MRI data are recorded on physically different computers with a possible mismatch in system time, the sequence was modified to transmit a synchronization trigger into the PET list-mode stream immediately before the first readout of the MRI data acquisition. This trigger defines a common reference time point, allowing to perform PET gating based on the time and gate information of the MRI SGS.

2.2. MR-based motion modeling

A nonrigid registration algorithm that was recently proposed for lung registration (Heinrich et al., 2012) is employed to compute the deformation between the N_{Bins} different, respiratory-gated MRI volumes. Empirically determined parameters for the deformable registration were smoothing $\alpha = 65.0\%$, 85% randomized sampling, and 3 levels with a grid spacing of 6, 4, and 2. Its output is a 3D deformation field $\mathcal{T}_{i,j}$ that contains the voxel-wise displacement

mapping from a volume at respiratory phase i to a volume at respiratory phase j , with $i, j \in \{1, \dots, N_{\text{Bins}}\}$. Phase 1 is defined as maximal expiration. The deformations are estimated from the μ -map phase, i.e., end-expiration, to all other phases, and from each respiratory phase to a reference volume. The reference volume is a self-gated reconstruction using a fixed amount of the data (here: 40%) with the most consistent amplitude in the self-gating signal, representing the most frequently visited respiratory position, which is most often close to end-expiration. This method is also referred to as *optimal gating* (van Elmpt et al., 2011). Thus, the required deformations are $\mathcal{T}_{1,i}$ and $\mathcal{T}_{i,ref} \forall i \in \{1, \dots, N_{\text{Bins}}\}$.

2.3. PET imaging and motion compensation

The deformations are applied, firstly, to generate matching μ -maps \mathbf{U}_i for the respiratory phases $i \in \{2, \dots, N_{\text{Bins}}\}$. The original end-exhale μ -map \mathbf{U} is warped to each respiratory state using the corresponding deformation field $\mathcal{T}_{1,i}$:

$$\mathbf{U}_i = \mathcal{T}_{1,i}(\mathbf{U}).$$

Secondly, the self-gating signal from the MRI acquisition is applied to reconstruct gated images \mathbf{x}_i from the PET list-mode data. A custom software tool was used to insert respiratory gating tagwords into the original list-mode file, according to the binning table of all SGS samples and the respective timestamps. Thus, N_{Bins} gated list-mode frames \mathbf{y}_i are generated that can be processed using the respiratory gating functionality in the vendor-supplied PET reconstruction software. The provided clinical implementation (3D ordered-subset expectation maximization, OSEM3D) is applied as reconstruction algorithm \mathcal{P} . The matching μ -maps are utilized for attenuation correction:

$$\mathbf{x}_i = \mathcal{P}(\mathbf{y}_i, \mathbf{U}_i).$$

Finally, the gates are co-registered by applying the deformation fields $\mathcal{T}_{i,ref}$ and then combined into the motion-compensated PET volume \mathbf{x} :

$$\mathbf{x} = \sum_{i=1}^{N_{\text{Bins}}} w_i \mathcal{T}_{i,\text{ref}}(\mathbf{x}_i).$$

Similar to the registration-weighted combination approach proposed by Dikaios and Fryer (2012) and the count-based weighting by Würslin et al. (2013), we perform a convex combination where the weights w_i , with $\sum_i w_i = 1$, are proportional to the intra-bin amplitude range of the self-gating signal (ignoring the lowest and highest 5% in the first and last bin):

$$w_i = 1 - \frac{S_{i,\text{max}} - S_{i,\text{min}}}{S_{N_{\text{Bins}},\text{max}} - S_{1,\text{min}}},$$

where $S_{i,\text{min}/\text{max}}$ refers to the amplitude of the minimum/maximum SGS sample in bin i . This scheme gives higher weight to bins with a lower intra-bin motion.

Thus, the whole motion-compensation process based on the list-mode gates \mathbf{y}_i and a static μ -map \mathbf{U} can be summarized as follows:

$$\mathbf{x} = \sum_{i=1}^{N_{\text{Bins}}} w_i \mathcal{T}_{i,\text{ref}}(\mathcal{P}(\mathbf{y}_i, \mathcal{T}_{1,i}(\mathbf{U}))).$$

For each patient, the following PET reconstructions were computed, focusing on a motion-compensated reconstruction based on $N_{\text{Bins}} = 5$ for the rest of the study:

1. R_{100} : Ungated reconstruction using all PET data and original μ -map.
2. R_{40} : Gated reconstruction using the 40% of the data with the least variation in the SGS amplitude.
3. G_5 : Proposed method – gating by 5 bins, post-reconstruction registration.

The reconstruction R_{40} serves as our gold standard and corresponds to the same optimal gating scheme as applied in the computation of the MRI reference volume for co-registration.

3. Experimental evaluation

The capabilities of the MRI motion model were assessed in three experiments using data from fifteen oncological patients P_1 – P_{15} with lesions in the chest or abdomen. All scans were conducted on a 3 Tesla integrated PET/MRI system (Biograph mMR; Siemens Healthcare, Erlangen, Germany) according to the scan protocol described in Section 2. Written consent from the subjects and approval from the local ethics committee was obtained prior to the examinations.

The following MRI acquisition parameters were used for a fat-suppressed, radial stack-of-stars GRE pulse sequence: TR/TE = 3.75/1.7 ms, field-of-view (FOV) $400 \times 400 \times 360 \text{ mm}^3$, spatial resolution $1.65 \times 1.65 \times 5 \text{ mm}^3$, $N_x = N_y = 256$ pixel matrix, $N_z = 72$ slices (61% slice resolution, 5/8 partial Fourier), 4416 radial angles, 10 min scan time. Images were reconstructed by regridding (Jackson et al., 1991).

For PET imaging in P_1 – P_{13} , a weight-adjusted dose of ^{18}F -FDG ($332 \pm 71 \text{ MBq}$; min: 236 MBq; max: 455 MBq) was administered as radionuclide agent, 102–155 min before the study. For P_{14} , P_{15} , 93/122 MBq of ^{68}Ga -DOTANOC were administered 52/66 min before the start of the simultaneous acquisition.

Only list-mode events recorded during the 10 min run time of the self-gated MRI sequence were considered. PET reconstruction was performed with standard clinical parameters (Drzezga et al., 2012): OSEM3D with 3 iterations on 21 subsets, with a matrix size of 172×172 , 127 slices (voxel size $4.17 \times 4.17 \times 2.03 \text{ mm}^3$), and 4 mm Gaussian post-reconstruction filtering. The maximum-likelihood reconstruction of attenuation and activity (Nuys et al.,

2013) was used to compensate for truncation of the arms in the μ -maps.

The first evaluation aimed at determining an appropriate value for N_{Bins} based on the apparent motion in the MR images. The second experiment studied the effect of reducing the MRI scan time on the resulting motion model, for $N_{\text{Bins}} = 5$. In the third experiment, the proposed approach for PET respiratory motion compensation was compared qualitatively and quantitatively against ungated and gated reconstructions, also using 5 respiratory bins.

3.1. Number of bins

For all patients, gated MR images were reconstructed using $N_{\text{Bins}} \in \{2, \dots, 15\}$ respiratory bins. Partitioning the data into more bins reduces the SNR in every bin and increases the streaking artifact level, but allows more accurate separation of different respiratory states. In radial k -space trajectories, streak artifacts are predominantly caused by undersampling (with respect to the Nyquist theorem). This occurs for $N_{\text{Bins}} \geq 11$, when less than 400 radial spokes are used to reconstruct a single bin for the described MRI protocol, or possibly earlier when the distribution of the acquired angles deviates much from uniformity. A virtual 1D navigator column along the head-foot direction was extracted close to the apex of the liver dome in the reconstructed volumes. The position of the liver edge at each respiratory state was detected by applying a threshold of 50% of the image-intensity difference between lung and liver parenchyma. These edge positions were used to determine the minimum number of respiratory bins that need to be used to ensure that the respiratory motion is sufficiently captured.

The number of bins chosen determines the apparent respiratory amplitude or detected maximum displacement d_{max} :

$$d_{\text{max}}(N_{\text{Bins}}) = |p_{N_{\text{Bins}}} - p_1|,$$

where $p_{N_{\text{Bins}}}$ and p_1 denote the detected liver edge positions in the end-inspiration and end-expiration bins, respectively. Due to the radial sampling scheme, residual intra-bin motion leads to blurring in the MR images, which causes d_{max} to appear smaller with a reduced number of bins.

To assess the impact on the observed displacement of the liver edge in all respiratory phases, the average binning error $B(N_{\text{Bins}})$ was computed as

$$B(N_{\text{Bins}}) = \frac{1}{15} \sum_{b=1}^{15} |p_b^{N_{\text{Bins}}} - p_b^{15}|,$$

where p_b^B denotes the liver edge position for Bin b out of 15 for a self-gated reconstruction with B bins. Nearest-neighbor interpolation was used to re-sample the edge positions to 15 bins for $N_{\text{Bins}} < 15$. Thus, the score B represents the average deviation of the reconstruction with a reduced number of bins from the reference $N_{\text{Bins}} = 15$.

3.2. Effect of MRI scan time on motion model

To further study the required minimum scan time for motion modeling, additional 5-bin reconstructions were computed that utilized only the first 1, 2, ..., 9 min of the acquired MRI data. Motion fields were estimated and resampled to the PET resolution and field of view. Using the motion fields from the full, 10 min scan as a reference, the mean squared error (MSE) was computed for all fields derived from the shortened scans and normalized, for each dataset, with respect to the error of the 9 min scan which we considered comparable to a full scan.

Furthermore, also the effect of shortening the MRI scan time on the resulting motion-compensated PET images was analyzed. For this purpose, the previously described motion models from a scan

time of $\{1, \dots, 10\}$ min were used for motion compensation in the post-reconstruction registration of G_5 . It is important to note here that only different deformation fields were applied, but the underlying gated PET images were identical for all tested MRI scan times. Using the result from the full motion model scan as reference, the MSE and structural similarity (SSIM) (Wang et al., 2004) were computed for the shortened scans. Again, the errors were normalized with respect to the difference between the results obtained with a scan time of 9 min and 10 min.

3.3. Effect of motion compensation on PET images

The resulting motion-compensated reconstructions based on the 10 min MRI scan and $N_{\text{Bins}} = 5$ were analyzed visually as well as quantitatively. In total, 39 moving lesions with focal tracer uptake were identified and enclosed by ellipsoidal volumes of interest (VOIs) in Amide 1.0.4. (Loening and Gambhir, 2003). Non-moving lesions were found only in three patients and not analyzed due to the insufficient sample size. An overview of the VOIs is given in Table 2. Additionally, for every dataset, a 30 mm³ spherical VOI was placed in the liver and a 25 × 15 × 35 mm³ cuboid VOI was placed in a vertebra for SNR analysis. The VOI voxels were exported and processed using custom software written in Matlab (The MathWorks Inc., Natick, MA). Lesions were characterized in terms of two widely used metrics, namely the maximum standardized uptake value (SUV_{max}) in the VOI and the mean SUV (SUV_{mean}), as well as the volume. The SUV_{mean} and volume were estimated as the average SUV and volume of the voxels in the VOI, respectively, considering only voxels with a value exceeding a certain threshold. The following thresholds were applied separately for every VOI:

- θ_{50} : $\geq 50\%$ of VOI-SUV_{max} per reconstruction.
- $\theta_{R_{100-50}}$: $\geq 50\%$ of VOI-SUV_{max} in R_{100} .

Moreover, cranio-caudal line profiles across the location of the voxel with SUV_{max} in R_{40} were interpolated to a resolution of 0.5 mm, cropped to only the section within the VOI, and evaluated for all reconstructions. Here, the full width at half maximum (FWHM) was computed, where “half maximum” refers to the mean of the respective maximum and baseline uptake. The average intensity at the beginning and end of each profile was considered as baseline. Similarly, lesion contrast was defined as the ratio between SUV_{max} and the baseline. Finally, the slope of the ascending and descending sections of each profile, between 20% and 80% of the maximum amplitude, again with respect to the baseline, were computed.

Table 2
Number, volume and location of lesion VOIs across patients.

Patient no.	Moving lesions	Total VOI volume (cm ³)	Location
P ₁	1	221	Liver dome
P ₂	1	19	Kidney medulla
P ₃	1	269	Lung, middle lobe
P ₄	13	250	Pancreas, liver metastases
P ₅	1	14	Ribs
P ₆	3	28	Liver, segment V
P ₇	1	217	Liver, segment VI
P ₈	2	52	Lung, middle; mediastinum
P ₉	0	n.a.	Lymph node (non-moving)
P ₁₀	1	11	Mediastinum
P ₁₁	1	26	Lung, hilar
P ₁₂	4	27	Thyroid, mediastinum
P ₁₃	1	120	Lung, upper lobe
P ₁₄	1	27	Liver, segment III
P ₁₅	6	107	Liver, various segments

The relative error was computed for all lesion evaluations. For SUV_{max}, SUV_{mean}, volume, and the profile measurements, R_{40} was considered as the reference, as these values can be assumed most accurate in a respiratory-gated reconstruction. For instance, the difference $\Delta_{\text{SUVmax}}(G_5)$ in SUV_{max} between G_5 and the reference was computed as

$$\Delta_{\text{SUVmax}}(G_5) = \frac{\text{SUV}_{\text{max}}(G_5) - \text{SUV}_{\text{max}}(R_{40})}{\text{SUV}_{\text{max}}(R_{40})}.$$

For the lesion volume estimation based on $\theta_{R_{100-50}}$, the magnitude of the relative error is given, due to the inconsistent trend to under- or overestimation:

$$\Delta_{\text{Vol}}(G_5) = \frac{|\text{Vol}(G_5) - \text{Vol}(R_{40})|}{\text{Vol}(R_{40})}.$$

The signal-to-noise ratio was defined as the mean over standard deviation in the respective regions in the spine and the liver. For the SNR comparison, R_{100} was considered the reference and G_5 and R_{40} were compared:

$$\Delta_{\text{SNR}}(G_5) = \frac{\text{SNR}(G_5) - \text{SNR}(R_{100})}{\text{SNR}(R_{100})}.$$

Statistical significance of the results was evaluated by the paired Wilcoxon signed-rank test implemented in the R software (R Development Core Team, 2010).

4. Results

4.1. Number of bins for MRI self-gating

In all cases, the self-gating signal was successfully extracted. The respiratory bins 1, 3, and 5 of 5 for patient P_{13} are shown in Fig. 3. The self-gating signal as well as the extracted virtual navigator columns for patients P_{12} and P_4 and $N_{\text{Bins}} = 15$ are depicted in Fig. 4.

In the experiments concerning the minimum number of bins, an asymptotic recovery of the apparent respiratory amplitude was observed. This is caused by successive reduction of intra-bin motion with a higher number of bins (Dawood et al., 2009), due to the uniform bin size. An overview of all patients is given in Fig. 5(a). The maximum displacement in the fifteen patients was 34 mm, the average was 18.9 ± 7.0 mm. If particularly deep inspiration occurred in few respiratory cycles, as it was the case for P_4 (Fig. 4(b)), 10 or more bins may be needed to recover the full respiratory amplitude. As illustrated in the box plot in Fig. 5(b), the average binning error B across all patients decreased rapidly until $N_{\text{Bins}} = 5$, after which the improvements became more gradual. In particular, the 95th percentile fell below the PET slice thickness of 2.1 mm for $N_{\text{Bins}} \geq 5$. Therefore, we recommend at least 5 bins to capture most of the expected motion.

4.2. Effect of MRI scan time on motion model

The decreasing sampling rate led to increased streaking, in particular for scan times of 1–3 min. Example reconstructions for the end-expiratory bin of P_{12} for different scan times are depicted in Fig. 6. With a reduced scan time of 7 or 8 min, the estimated fields were close to the 9 min and full scan, as shown in the box plot in Fig. 7. A further reduction to 4–6 min of scan time introduced moderate deviations, while a scan time of 1–2 min appeared unstable. This indicates that although the visual image quality is degraded in the undersampled scans, the registration algorithm tolerates also a significantly shortened scan time. Note that differences in the deformation fields do not only originate from the increased artifact

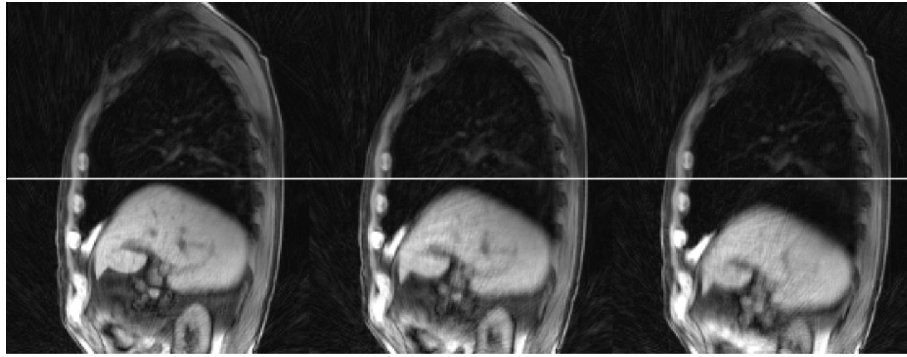


Fig. 3. Respiratory bins 1, 3, 5 for $P_{13}(N_{\text{Bins}} = 5)$.

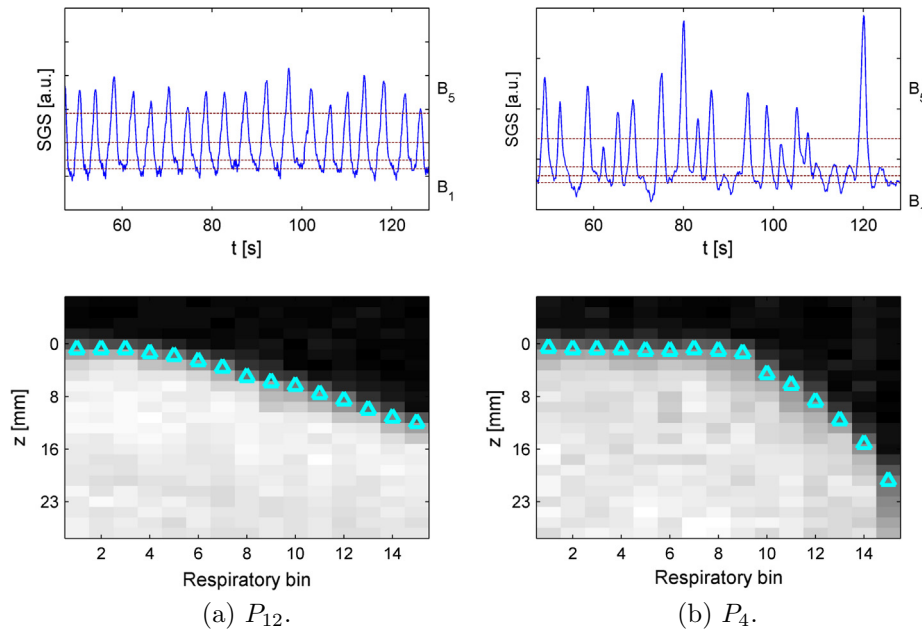


Fig. 4. Self-gating signal and virtual navigator for patients P_{12} and $P_4(N_{\text{Bins}} = 15)$. The boundaries of the bins B_i for $N_{\text{Bins}} = 5$ are indicated by the dashed horizontal lines in the SGS. Triangles mark the detected liver edge in the navigator. The amplitude, end-expiratory fraction and distribution of the respiratory phases are highly patient-specific.

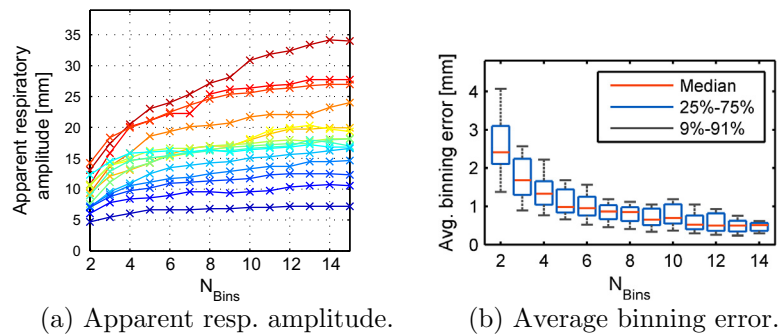


Fig. 5. Depending on the specific respiratory pattern, a high number of gating bins may be required to resolve the maximum apparent respiratory amplitude (a). Each line represents one patient. The average binning error (b) considers the error in the position of all respiratory bins and falls below the PET slice thickness of 2 mm for $N_{\text{Bins}} = 5$.

level, but may also be attributed to a change in the respiratory pattern, e.g., if the patient relaxes after a few minutes.

Both the MSE and SSIM indicated stability of the motion-compensated PET reconstruction using a model generated from reduced MRI scan times, as can be seen in Fig. 8. The MSE was generally lower than in the deformation fields. A possible explanation

is that streak artifacts in low-intensity regions in the MR image, such as in the surrounding air, can cause deviations in the deformation fields that do not affect the PET reconstruction (due to likewise low tracer uptake in those regions). Already 3–4 min of the self-gating MRI scan were sufficient to form a model that resulted in visually comparable motion-compensated PET images.

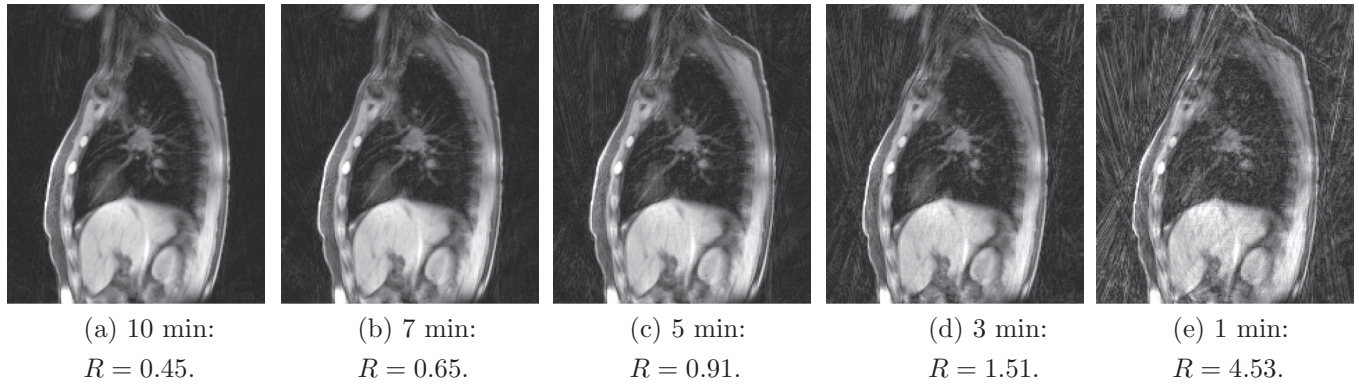


Fig. 6. Gated MRI reconstructions with shortened scan time (P_{12} , end-expiratory bin). The undersampling factor R corresponds to the degree of k -space undersampling with regard to full Nyquist sampling ($R = 1$: 400 radial spokes for images at 256 pixel resolution). $R < 1$ indicates oversampling.

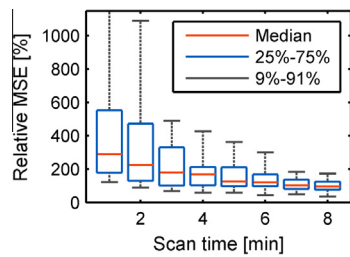


Fig. 7. Effect of shortened motion-modeling scan on the estimated deformation fields, relative to the difference between 9 min and 10 min scan time. With less than 3 min scan time, large deviations of the MSE occur, potentially caused by mis-registration due to the high level of streak artifacts.

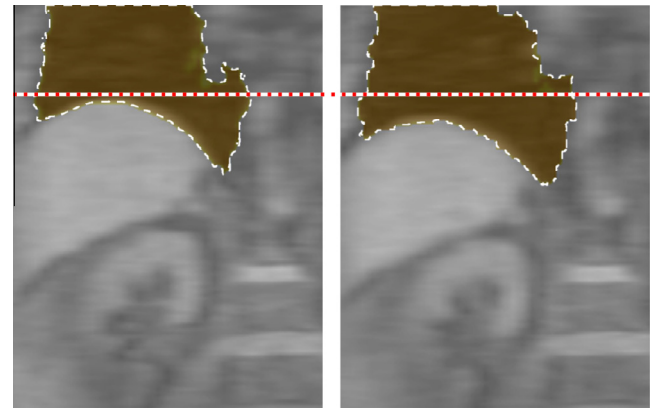


Fig. 9. Self-gated MRI of P_1 overlaid with original μ -map at end-expiration (U_1 , left) (brown: lung compartment) and the warped μ -map at end-inspiration (U_5 , right). In both phases, the edges of the μ -map match the anatomy. (For interpretation of the references to color in this figure legend, the reader is referred to the web version of this article.)

With 2 min or less, the difference in the motion-compensated PET images increased, although only slight local distortions were noticed visually.

4.3. Motion-compensated PET reconstruction

When overlaying the motion model with the Dixon images acquired for the μ -map, it was noticed that five of the patients had held their breath at end-inspiration rather than at end-expiration as instructed. In these cases, the deformation fields ($\mathcal{T}_{5,i}$) using the end-inspiratory phase as reference had to be computed in order to generate the deformed μ -maps:

$$U_i = \mathcal{T}_{5,i}(U).$$

Similarly, the end-exhale μ -map for reconstructions R_{100} , R_{40} was estimated by applying $\mathcal{T}_{5,1}$. After that, the tissue interfaces in the deformed μ -maps were visually consistent with the acquired motion model. An exemplary fusion of the motion model at end-expiration and end-inspiration with the corresponding μ -maps in P_1 is depicted in Fig. 9.

The weights for averaging the co-registered PET reconstructions were largest in the second bin, with an average of 0.23 ± 0.006 , as shown in the box plot in Fig. 10. The bin at end-inspiration typi-

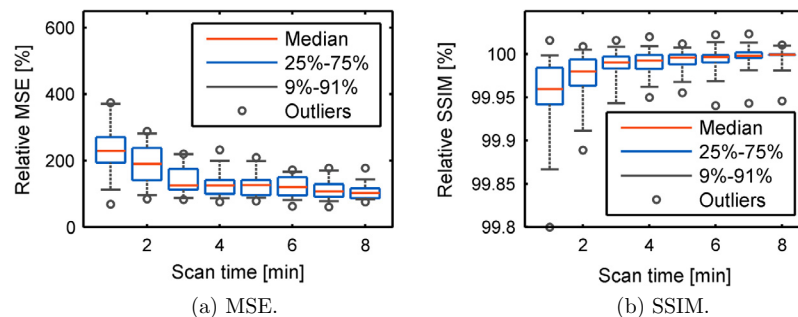


Fig. 8. Effect of shortened motion-modeling scan on the motion-compensated PET reconstruction, relative to the difference between 9 min and 10 min scan time. The deviations of the deformation fields with short scan times of 1–2 min (see Fig. 7) also translate into deviations of the resulting motion-compensated reconstruction. With a scan time of 3–4 min or longer, the reconstructions are comparable to the result based on a 10 min scan.

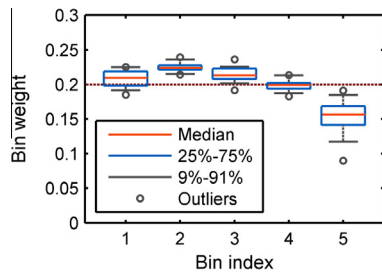


Fig. 10. Distribution of bin weights, computed as the reciprocal of the relative intra-bin variance. The dotted horizontal line at 0.2 marks the uniform weight for $N_{\text{Bins}} = 5$. Bin 2 was, on average, weighted highest, while the end-inspiratory Bin 5 was typically assigned the lowest weight. Thus, the influence of phases with large expected intra-bin motion is mitigated.

cally received the lowest weight, with an average of 0.15 ± 0.026 . Thus, its contribution is weakened, as this bin is typically affected by residual intra-bin motion.

An example of the reconstruction results is given in Fig. 11a–d, showing a sagittal slice through the heart and a lesion in the lung of P_8 . The ventricle walls as well as the lesion are blurred in the ungated reconstruction, and improved sharpness is evident in both the gated and the corrected reconstructions. The plots in Fig. 11e and f show line profiles through the lesion and the right ventricle of P_8 for the three reconstructions. In both profiles, only minimal differences between the motion-compensated reconstruction G_5 and R_{40} are seen, whereas R_{100} appears smoothed and stretched due to motion.

All results from the quantitative evaluation of the motion-compensation accuracy are summarized in Table 3. The reconstructions exhibited a distinct trend: The SUV_{max} , SUV_{mean} , profile contrast, and slope (39 up- and downslopes, respectively) observed in R_{40} were larger than in both other reconstructions in virtually all lesions. However, the corresponding estimations in G_5 were generally larger than in R_{100} . Similarly, the lesion volume according to θ_{50} and FWHM appeared smallest in R_{40} and largest in R_{100} . The lesion volume estimations based on the fixed threshold $\theta_{R_{100}-50}$ were less consistent, indicating possible under- or overestimation of the volume in the static and motion-compensated reconstructions. The SNR was clearly lowest in R_{40} , and highest in R_{100} . For the patients examined with the ^{68}Ga -DOTANOC tracer, only marginal uptake

Table 3

Overview of lesion quantification results. Each column indicates in how many of the 39 (slope: 78) cases the corresponding measured quantity was larger in one reconstruction than in another.

Number of cases	$R_{40} > R_{100}$	$R_{40} > G_5$	$G_5 > R_{100}$
Lesion SUV_{max}	39	39	30
Lesion $\text{SUV}_{\text{mean}}(\theta_{50})$	39	38	29
Lesion $\text{SUV}_{\text{mean}}(\theta_{R_{100}-50})$	38	35	27
Lesion vol. (θ_{50})	1	4	2
Lesion vol. ($\theta_{R_{100}-50}$)	20	33	11
Profile FWHM	2	12	6
Profile contrast	38	35	37
Profile up- and downslope	77	66	64
Liver SNR	0	0	14
Spine SNR	0	0	4

was observed in the spine. The vertebral VOIs of these two cases were therefore excluded from the SNR analysis.

The average relative difference with respect to the reference reconstruction is presented in Table 4. The proposed method, G_5 , achieved a significant improvement in the accuracy for all of the examined quantitative measures and typical indicators for the clarity of lesion depiction, compared to the ungated reconstruction R_{100} . The sharpness and SUV quantification of the gated reconstruction R_{40} was not fully met by G_5 . However, G_5 was not associated with the SNR loss of 18–35% that affected R_{40} . On the contrary, an increase in SNR by 7% was observed in the liver, potentially due to the interpolation step during image fusion.

5. Discussion

To summarize our key findings, the use of a self-gated stack-of-stars MRI sequence for the purpose of respiratory motion modeling was demonstrated. The first experiment led to the conclusion that gating should use at least 5 bins to reduce most of the intra-bin motion at the diaphragm. The second experiment revealed that for the purpose of motion modeling with 5 bins, 3–5 min of MRI scan time are sufficient. Finally, quantitative analysis in the third experiment showed that PET respiratory motion compensation is feasible with the proposed method. Compared to an ungated reconstruction, the lesion quantification accuracy and sharpness were improved, while, compared to a gated reconstruction, a high

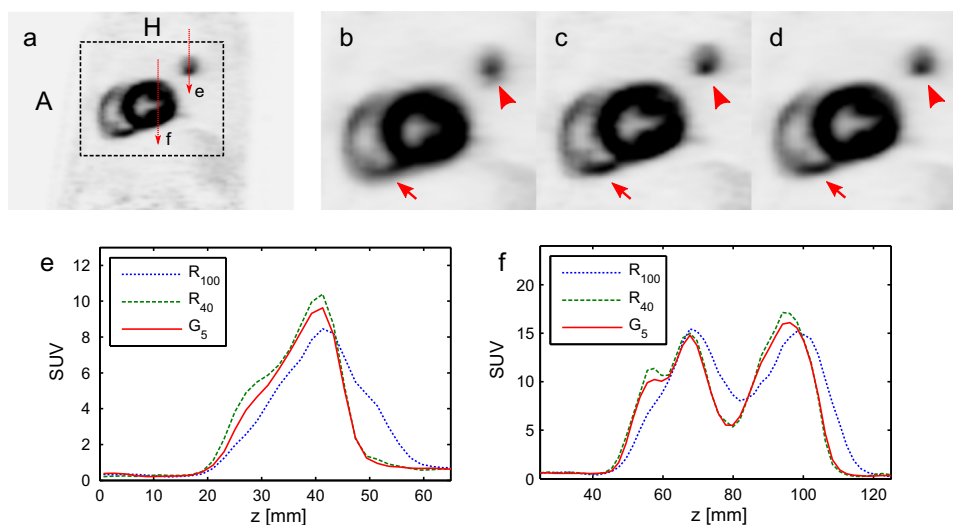


Fig. 11. (a) Sagittal slice through heart and lesion in PET of P_8 . Zoomed region: (b) R_{100} , (c) R_{40} , (d) G_5 . The lesion (arrowhead) appears stretched in the ungated image, and its true, drop-shaped profile is not captured correctly. The right-ventricle wall (arrow) is blurred. Both features are improved in the motion-compensated reconstruction. This is also seen in the line profiles through (e) the lesion and (f) the myocardium.

Table 4Average relative difference in lesions and in profiles with respect to R_{40} , and in SNR with respect to R_{100} .

Relative difference (Reference: R_{40})	R_{100}		G_5 (Proposed)		P
	Mean (%)	Std (%)	Mean (%)	Std (%)	
Lesion SUV_{max}	-13.6	7.4	-9.3	4.5	<0.001
$SUV_{mean}(\theta_{50})$	-13.5	7.4	-9.5	5.4	0.001
$SUV_{mean}(\theta_{R100-50})$	-4.8	3.1	-3.5	2.9	0.004
Volume (θ_{50})	58.7	62.6	23.0	27.3	<0.001
Volume ($\theta_{R100-50}$)	11.5	10.7	9.4	7.3	<0.001
Profile FWHM	14.9	18.3	6.5	15.4	<0.001
Profile Contrast	-24.3	13.9	-10.3	12.0	<0.001
Profile Slope	-29.8	19.6	-16.1	16.7	<0.001
Relative difference (Reference: R_{100})	R_{40}		G_5 (Proposed)		P
	Mean	Std	Mean	Std	
Liver SNR	-34.5	7.2	6.8	8.2	0.001
Spine SNR	-17.9	9.2	0.0	2.2	<0.001

SNR was maintained. The presented study is a first step towards a systematically evaluated protocol for MRI-based motion compensation of PET images. When implementing such techniques, it is important to consider some fundamental points of discussion that will be identified in the following.

5.1. Optimal number of bins

The optimal number of bins to be differentiated, subject of our Experiment Section 3.1, depends on three patient-specific factors: Firstly, the amount of blurring due to respiration depends on the maximum respiratory amplitude. With a larger amplitude, more bins may be required (Dawood et al., 2009). Secondly, the (inter-bin) distribution of the respiratory phases is important (Liu et al., 2009). The more time is spent in a quiescent period at end-exhalation, the smaller is the fraction of the acquisition time affected by motion that needs to be compensated for. Thirdly, if no data should be discarded and the number of bins is limited, intra-bin motion blurring particularly at end-inspiration and in the presence of irregular breathing cannot be avoided and also contributes to the combined, motion-compensated PET image. Thus, the choice of a fixed number of bins has to be seen as a compromise: While the use of too few bins may prohibit complete compensation of the respiratory motion, a high number of bins always comes at increased computational complexity but does not necessarily yield further improvements. The results in our study population indicate that with 5 or more bins, the average binning error falls below the PET slice thickness. At least for PRR-based motion compensation, the PET count rate can also impose an upper limit for the number of respiratory bins. A sufficient coincidence count in every bin should be met to ensure stability of the reconstruction algorithm.

A possible starting point for patient-individual compensation strategies is a classification of the respiratory pattern, e.g., into the three characteristic distribution groups identified by Liu et al. (2009) and Polycarpou et al. (2014), who distinguish between (1) respiration with a quiescent peak at end-expiration, (2) with a Gaussian or Poisson-like distribution, and (3) an approximately uniform distribution of respiratory phases. A group-specific number of respiratory bins could be utilized, possibly combined with discarding PET data at respiratory outliers such as singular deep inspiration.

A limitation of this study is the fact that the evaluation of the optimal number of bins focused on the effect of detected liver edge positions in the gated MRI volumes. The effect of a varying number of bins on the depiction of lesions remains to be examined in future work. Since the result also depends on the variance in lesion location, size, and motility, a larger patient population or restriction to lesions in a specific organ may be desirable for such experiments.

However, since our recommendations were derived from the diaphragm displacement that indicates the maximum expected lesion motion range, the result can be considered a conservative estimate that is not biased by the lesion location.

5.2. MRI scan time

A question related to the optimal number of bins is the actually required MRI scan time that was evaluated in Experiment Section 3.2. Despite the advantage of capturing the global course of respiration during the examination, the long scan time of 10 min dedicated for motion modeling prevents other diagnostic MRI scans during this time. Addressing this could improve clinical acceptance. One argument in justifying the self-gated MRI scan time is that the resulting MR images can provide diagnostic information in addition to the deformation fields. The T1-weighted image contrast obtained with the utilized radial MRI sequence in combination with simultaneously acquired PET has been shown to be highly sensitive in the detection of FDG-avid nodules (Chandarana et al., 2013).

As shown in the second experiment, a reduction of the MRI scan time is easily possible by acquiring fewer radial spokes at the cost of increased radial streaking artifacts. Already in the present implementation, both the deformation fields and the resulting motion-compensated PET image volumes indicate that a scan time of 3–4 min may be sufficient for MRI motion modeling. Robust registration methods, on the one hand, and Compressed Sensing reconstruction of the MRI images (Feng et al., 2013), on the other hand, can help to further increase the tolerance of undersampling artifacts.

When shortening the MRI scan, the physiological signal needs to be derived by other means, e.g., by a belt or bellows, or using PET-based self-gating (Büther et al., 2009; Schleyer et al., 2009), for the remaining list-mode acquisition after the motion modeling phase. Thus, after validating the correspondence between the MR-based motion model and the physiological signal surrogate, motion-compensated PET imaging could also be applied while conducting other routine MRI examinations.

5.3. Comparison with related work

The results of the presented evaluation are in accordance to the previous work listed in Table 1, in the sense that motion compensation generally helps to reduce motion-related artifacts. With regard to the number of bins, the value of $N_{Bins} = 8$ used by Dikaos et al. (2012) and Dutta et al. (2013) seems conservative, and a reduced number of bins could have been sufficient. Ouyang et al. (2013) utilized also 8 bins, but distinguished between inspiratory and expiratory phases. Similarly, the choice of $N_{Bins} = 4$ by

Würslin et al. (2013) may have led to a limited amount of residual motion, depending on the patient-specific respiration. For an average respiratory cycle length of 5 s, the intra-bin motion with our exemplary value of $N_{\text{bins}} = 5$ corresponds to a temporal resolution of about 500 ms in a fast MRI acquisition, since hysteresis effects are neglected. This matches the temporal resolution used by Buerger et al. (2012b). A comparison of the individual quantitative results is, however, difficult due to the lack of consensus on important quantitative measures regarding motion blur, and due to differences in their detailed definition.

5.4. Gating or motion compensation?

The clearly increased lesion sharpness in R_{40} in Experiment Section 3.3 confirms that the MRI-based self-gating signal is a viable physiological surrogate signal for the purpose of respiratory gating. As also observed by Würslin et al. (2013), motion compensation does improve but not fully restore the lesion SUV_{max} , SUV_{mean} , FWHM, contrast, and slope. By definition, when a suitable gating tolerance is used, a motion-compensated method that combines multiple gates is always subject to more residual motion than a single gated reconstruction. A limited loss of sharpness is inevitable due to residual motion in the end-inspiratory bin, registration inaccuracies, and the applied interpolation. It should, however, also be borne in mind that R_{40} , which served as our reference, is not perfect ground truth. The higher noise level due to gating is known to cause, for instance, overestimation of SUV_{max} (Liu et al., 2010), which consequently also affects most of the other examined quantitative measures because they typically depend on SUV_{max} .

Ultimately, the choice of the optimal method for motion compensation also depends on the available PET scan time in the clinical protocol. On the one hand, if scan time is not a concern, a long respiratory-gated scan such as R_{40} provides optimal lesion sharpness. On the other hand, the total patient table time is often already long, in particular for hybrid PET/MRI. In such cases, the required additional scan time renders respiratory gating unattractive, so that the bed positions including chest and abdomen are acquired as quickly as possible, e.g., in 4 min. Traditionally, R_{100} would have been applied to avoid insufficient SNR. Here, a motion-compensated reconstruction such as G_5 can improve the quantification accuracy and conspicuity of lesions, while SNR is preserved.

6. Conclusion

We presented comprehensive in vivo results from self-gated MRI motion modeling applied to respiratory motion compensation for PET imaging on integrated PET/MRI systems. Self-gated MRI requires no additional physiological signal sensors and captures image volumes of the averaged respiratory motion cycle throughout the measurement. Hence, it is a convenient method for retrospectively gated reconstruction. To eliminate most of the intra-bin motion, at least 5 bins should be used. For a configuration using 5 bins, a scan time of 3–4 min is sufficient to form the motion model.

The robustness of the approach was demonstrated in a study of 15 oncological patients with lesions of different sizes in the chest and abdomen. The motion model was used to correct for respiratory motion in PET reconstructions, resulting in reduced motion blur and improved quantification accuracy compared to static reconstructions and in higher SNR compared to conventional gated reconstructions.

Acknowledgements

The authors gratefully acknowledge helpful discussions with and the technical assistance of Simon Bauer and Matthias Fenchel,

both from Siemens Healthcare, MR Application Development. Moreover, we thank Markus Schwaiger (Klinikum Rechts der Isar, TUM) for supporting the studies at his institution.

References

- Buerger, C., Clough, R.E., King, A.P., Schaeffter, T., Prieto, C., 2012a. Nonrigid motion modeling of the liver from 3-d undersampled self-gated golden-radial phase encoded MRI. *IEEE Trans. Med. Imag.* 31, 805–815. <http://dx.doi.org/10.1109/TMI.2011.2181997>.
- Buerger, C., Tsoumpas, C., Aitken, A., King, A.P., Schleyer, P., Schulz, V., Marsden, P.K., Schaeffter, T., 2012b. Investigation of MR-based attenuation correction and motion compensation for hybrid PET/MR. *IEEE Trans. Nucl. Sci.* 59, 1967–1976. <http://dx.doi.org/10.1109/TNS.2012.2209127>.
- Bundschuh, R.A., Martínez-Möller, A., Essler, M., Nekolla, S.G., Ziegler, S.I., Schwaiger, M., 2008. Local motion correction for lung tumours in PET/CT – first results. *Eur. J. Nucl. Med. Mol. Imag.* 35, 1981–1988. <http://dx.doi.org/10.1007/s00259-008-0868-0>.
- Büther, F., Dawood, M., Stegger, L., Wübbeling, F., Schäfers, M., Schober, O., Schäfers, M., 2009. List mode-driven cardiac and respiratory gating in PET. *J. Nucl. Med.* 50, 674–681. <http://dx.doi.org/10.2967/jnumed.108.059204>.
- Chandarana, H., Block, T.K., Rosenkrantz, A.B., Lim, R.P., Kim, D., Mossa, D.J., Babb, J.S., Kiefer, B., Lee, V.S., 2011. Free-breathing radial 3d fat-suppressed T1-weighted gradient echo sequence: a viable alternative for contrast-enhanced liver imaging in patients unable to suspend respiration. *Invest. Radiol.* 46, 648–653. <http://dx.doi.org/10.1097/RLI.0b013e31821eea45>.
- Chandarana, H., Heacock, L., Rakheja, R., Demello, L.R., Bonavita, J., Block, K.T., Geppert, C., Babb, J.S., Friedman, K.P., 2013. Pulmonary nodules in patients with primary malignancy: comparison of hybrid PET/MR and PET/CT imaging. *Radiology* 268, 874–881. <http://dx.doi.org/10.1148/radiol.13130620>.
- Chun, S., Fessler, J., 2013. Noise properties of motion-compensated tomographic image reconstruction methods. *IEEE Trans. Med. Imag.* 32, 141–152. <http://dx.doi.org/10.1109/TMI.2012.2206604>.
- Chun, S.Y., Reese, T.G., Ouyang, J., Guérin, B., Catana, C., Zhu, X., Alpert, N.M., El Fakhri, G., 2012. MRI-based nonrigid motion correction in simultaneous PET/MRI. *J. Nucl. Med.* 53, 1284–1291. <http://dx.doi.org/10.2967/jnumed.111.092353>.
- Dawood, M., Büther, F., Lang, N., Schober, O., Schäfers, K.P., 2007. Respiratory gating in positron emission tomography: a quantitative comparison of different gating schemes. *Med. Phys.* 34, 3067–3076. <http://dx.doi.org/10.1118/1.2748104>.
- Dawood, M., Büther, F., Stegger, L., Jiang, X., Schober, O., Schäfers, M., Schäfers, K.P., 2009. Optimal number of respiratory gates in positron emission tomography: a cardiac patient study. *Med. Phys.* 36, 1775–1784. <http://dx.doi.org/10.1118/1.3112422>.
- Delso, G., Fürst, S., Jakoby, B., Ladebeck, R., Ganter, C., Nekolla, S.G., Schwaiger, M., Ziegler, S.I., 2011. Performance measurements of the Siemens mMR integrated whole-body PET/MR scanner. *J. Nucl. Med.* 52, 1914–1922. <http://dx.doi.org/10.2967/jnumed.111.092726>.
- Dikaos, N., Fryer, T.D., 2011. Acceleration of motion-compensated PET reconstruction: ordered subsets-gates EM algorithms and a priori reference gate information. *Phys. Med. Biol.* 56, 1695–1715. <http://dx.doi.org/10.1088/0031-9155/56/6/011>.
- Dikaos, N., Fryer, T.D., 2012. Registration-weighted motion correction for PET. *Med. Phys.* 39, 1253–1264. <http://dx.doi.org/10.1118/1.3675922>.
- Dikaos, N., Izquierdo-Garcia, D., Graves, M.J., Mani, V., Fayad, Z.A., Fryer, T.D., 2012. MRI-based motion correction of thoracic PET: initial comparison of acquisition protocols and correction strategies suitable for simultaneous PET/MRI systems. *Eur. Radiol.* 22, 439–446. <http://dx.doi.org/10.1007/s00330-011-2274-4>.
- Drzegza, A., Souvatzoglou, M., Eiber, M., Beer, A.J., Frst, S., Martinez-Mller, A., Nekolla, S.G., Ziegler, S., Ganter, C., Rummeny, E.J., Schwaiger, M., 2012. First clinical experience with integrated whole-body PET/MR: comparison to PET/CT in patients with oncologic diagnoses. *J. Nucl. Med.* 53, 845–855. <http://dx.doi.org/10.2967/jnumed.111.098608>.
- Dutta, J., El Fakhri, G., Huang, C., Petibon, Y., Reese, T.G., Li, Q., 2013. Respiratory motion compensation in simultaneous PET/mr using a maximum a posteriori approach. In: 2013 IEEE 10th International Symposium on Biomedical Imaging (ISBI). IEEE, pp. 800–803. <http://dx.doi.org/10.1109/ISBI.2013.6556596>.
- Feng, L., Liu, J., Block, K.T., Xu, J., Axel, L., Sodickson, D.K., Otazo, R., 2013. Compressed sensing reconstruction with an additional respiratory-phase dimension for free-breathing imaging. In: Proc. 21st Annual Meeting ISMRM, Salt Lake City, Utah, USA, pp. 0606.
- Geramifard, P., Zafarghandi, M.S., Ghafarian, P., Rahmim, A., Ay, M.R., 2013. Respiratory-induced errors in tumor quantification and delineation in CT attenuation-corrected PET images: effects of tumor size, tumor location, and respiratory trace: a simulation study using the 4d XCAT phantom. *Mol. Imag. Biol.* 15, 655–665. <http://dx.doi.org/10.1007/s11307-013-0656-5>.
- Grimm, R., Bauer, S., Kiefer, B., Hornegger, J., Block, K.T., 2013a. Optimal channel selection for respiratory self-gating signals. In: Proc. 21st Annual Meeting ISMRM, Salt Lake City, Utah, USA, pp. 3749.
- Grimm, R., Fürst, S., Dregely, I., Forman, C., Hutter, J., Ziegler, S.I., Nekolla, S.G., Kiefer, B., Schwaiger, M., Hornegger, J., Block, K.T., 2013b. Self-gated radial MRI for respiratory motion compensation on hybrid PET/MR systems. In: MICCAI (3), pp. 17–24. http://dx.doi.org/10.1007/978-3-642-40760-4_3.

- Guérin, B., Cho, S., Chun, S.Y., Zhu, X., Alpert, N.M., El Fakhri, G., Reese, T., Catana, C., 2011. Nonrigid PET motion compensation in the lower abdomen using simultaneous tagged-MRI and PET imaging. *Med. Phys.* 38, 3025–3038. <http://dx.doi.org/10.1118/1.3589136>.
- Heinrich, M.P., Jenkinson, M., Brady, M., Schnabel, J.A., 2012. Globally optimal deformable registration on a minimum spanning tree using dense displacement sampling. In: Ayache, N., Delingette, H., Golland, P., Mori, K. (Eds.), *MICCAI 2012*, Part III. Springer, pp. 115–122. http://dx.doi.org/10.1007/978-3-642-33454-2_15.
- Huang, C., Dutta, J., Petibon, Y., Reese, T.G., Li, Q., El Fakhri, G., 2013. A novel golden-angle radial FLASH motion-estimation sequence for simultaneous thoracic PET-MR. In: *Proc. Intl. Soc. Mag. Reson. Med.*, pp. 2684.
- Jackson, J.L., Meyer, C.H., Nishimura, D.G., Macovski, A., 1991. Selection of a convolution function for fourier inversion using gridding. *IEEE Trans. Med. Imag.* 10, 473–478. <http://dx.doi.org/10.1109/42.97598>.
- Keller, S.H., Holm, S., Hansen, A.E., Sattler, B., Andersen, F., Klausen, T.L., Højgaard, L., Kjær, A., Beyer, T., 2013. Image artifacts from MR-based attenuation correction in clinical, whole-body PET/MRI. *MAGMA* 26, 173–181. <http://dx.doi.org/10.1007/s10334-012-0345-4>.
- King, A.P., Buerger, C., Tsoumpas, C., Marsden, P.K., Schaeffter, T., 2012. Thoracic respiratory motion estimation from MRI using a statistical model and a 2-D image navigator. *Med. Image Anal.* 16, 252–264. <http://dx.doi.org/10.1016/j.media.2011.08.003>.
- Lamare, F., Ledesma Carbayo, M.J., Cresson, T., Kontaxakis, G., Santos, A., Le Rest, C.C., Reader, A.J., Visvikis, D., 2007. List-mode-based reconstruction for respiratory motion correction in PET using non-rigid body transformations. *Phys. Med. Biol.* 52, 5187–5204. <http://dx.doi.org/10.1088/0031-9155/52/17/006>.
- Lin, W., Guo, J., Rosen, M.A., Song, H.K., 2008. Respiratory motion-compensated radial dynamic contrast-enhanced (DCE)-MRI of chest and abdominal lesions. *Magn. Reson. Med.* 60, 1135–1146. <http://dx.doi.org/10.1002/mrm.21740>.
- Liu, C., Pierce, L.A., Alessio, A.M., Kinahan, P.E., 2009. The impact of respiratory motion on tumor quantification and delineation in static PET/CT imaging. *Phys. Med. Biol.* 54, 7345–7362. <http://dx.doi.org/10.1088/0031-9155/54/24/007>.
- Liu, C., Alessio, A., Pierce, L., Thielemans, K., Wollenweber, S., Ganin, A., Kinahan, P., 2010. Quiescent period respiratory gating for PET/CT. *Med. Phys.* 37, 5037–5043. <http://dx.doi.org/10.1118/1.3480508>.
- Loening, A.M., Gambhir, S.S., 2003. AMIDE: a free software tool for multimodality medical image analysis. *Mol. Imag.* 2, 131–137. <<http://amide.sourceforge.net>>.
- McClelland, J.R., Hawkes, D.J., Schaeffter, T., King, A.P., 2013. Respiratory motion models: a review. *Med. Image Anal.* 17, 19–42. <http://dx.doi.org/10.1016/j.media.2012.09.005>.
- Nehmeh, S.A., Erdi, Y.E., Ling, C.C., Rosenzweig, K.E., Squire, O.D., Braban, L.E., Ford, E., Sidhu, K., Mageras, G.S., Larson, S.M., Humm, J.L., 2002. Effect of respiratory gating on reducing lung motion artifacts in PET imaging of lung cancer. *Med. Phys.* 29, 366–371. <http://dx.doi.org/10.1118/1.1448824>.
- Nuyts, J., Bal, G., Kehren, F., Fenchel, M., Michel, C., Watson, C., 2013. Completion of a truncated attenuation image from the attenuated PET emission data. *IEEE Trans. Med. Imag.* 32, 237–246. <http://dx.doi.org/10.1109/TMI.2012.2220376>.
- Ouyang, J., Li, Q., El Fakhri, G., 2013. Magnetic resonance-based motion correction for positron emission tomography imaging. *Semin. Nucl. Med.* 43, 60–67. <http://dx.doi.org/10.1053/j.semnuclmed.2012.08.007>.
- Paul, J., Divkovic, E., Wundrak, S., Bernhardt, P., Rottbauer, W., Neumann, H., Rasche, V., 2014. High-resolution respiratory self-gated golden angle cardiac MRI: comparison of self-gating methods in combination with *k-t* SPARSE SENSE. *Magn. Reson. Med.* <http://dx.doi.org/10.1002/mrm.25102>.
- Polycarpou, I., Tsoumpas, C., Marsden, P.K., 2012. Analysis and comparison of two methods for motion correction in PET imaging. *Med. Phys.* 39, 6474–6483. <http://dx.doi.org/10.1118/1.4754586>.
- Polycarpou, I., Tsoumpas, C., King, A.P., Marsden, P.K., 2014. Impact of respiratory motion correction and spatial resolution on lesion detection in PET: a simulation study based on real MR dynamic data. *Phys. Med. Biol.* 59, 697. <http://dx.doi.org/10.1088/0031-9155/59/3/697>.
- Rahmim, A., Tang, J., Zaidi, H., 2013. Four-dimensional image reconstruction strategies in cardiac-gated and respiratory-gated PET imaging. *PET Clin.* 8, 51–67. <http://dx.doi.org/10.1016/j.cpet.2012.10.005>.
- R Development Core Team, 2010. *R: A Language and Environment for Statistical Computing*. R Foundation for Statistical Computing, Vienna, Austria, ISBN 3-900051-07-0.
- Schleyer, P.J., O'Doherty, M.J., Barrington, S.F., Marsden, P.K., 2009. Retrospective data-driven respiratory gating for PET/CT. *Phys. Med. Biol.* 54, 1935–1950. <http://dx.doi.org/10.1088/0031-9155/54/7/005>.
- Tsoumpas, C., Buerger, C., King, A.P., Mollet, P., Keereman, V., Vandenberghe, S., Schulz, V., Schleyer, P., Schaeffter, T., Marsden, P.K., 2011. Fast generation of 4D PET-MR data from real dynamic MR acquisitions. *Phys. Med. Biol.* 56, 6597–6613. <http://dx.doi.org/10.1088/0031-9155/56/20/005>.
- Tsoumpas, C., Polycarpou, I., Thielemans, K., Buerger, C., King, A.P., Schaeffter, T., Marsden, P.K., 2013. The effect of regularization in motion compensated PET image reconstruction: a realistic numerical 4d simulation study. *Phys. Med. Biol.* 58, 1759. <http://dx.doi.org/10.1088/0031-9155/58/6/1759>.
- van Elmpt, W., Hamill, J., Jones, J., Ruyscher, D., Lambin, P., Öllers, M., 2011. Optimal gating compared to 3d and 4d PET reconstruction for characterization of lung tumours. *Eur. J. Nucl. Med. Mol. Imag.* 38, 843–855. <http://dx.doi.org/10.1007/s00259-010-1716-6>.
- Wang, Z., Bovik, A.C., Sheikh, H.R., Simoncelli, E.P., 2004. Image quality assessment: from error visibility to structural similarity. *IEEE Trans. Image Process.* 13, 600–612. <http://dx.doi.org/10.1109/TIP.2003.819861>.
- Winkelmann, S., Schaeffter, T., Koehler, T., Eggers, H., Doessel, O., 2007. An optimal radial profile order based on the golden ratio for time-resolved MRI. *IEEE Trans. Med. Imag.* 26, 68–76. <http://dx.doi.org/10.1109/TMI.2006.885337>.
- Würslin, C., Schmidt, H., Martirosian, P., Brendle, C., Boss, A., Schwenzer, N.F., Stegger, L., 2013. Respiratory motion correction in oncologic PET using T1-weighted MR imaging on a simultaneous whole-body PET/MR system. *J. Nucl. Med.* 54, 464–471. <http://dx.doi.org/10.2967/jnumed.112.105296>.